

Least-squares migration in the presence of velocity errors

Simon Luo¹ and Dave Hale¹

ABSTRACT

Seismic migration requires an accurate background velocity model that correctly predicts the kinematics of wave propagation in the true subsurface. Least-squares migration, which seeks the inverse rather than the adjoint of a forward modeling operator, is especially sensitive to errors in this background model. This can result in traveltime differences between predicted and observed data that lead to incoherent and defocused migration images. We have developed an alternative misfit function for use in least-squares migration that measures amplitude differences between predicted and observed data, i.e., differences after correcting for nonzero traveltime shifts between predicted and observed data. We demonstrated on synthetic and field data that, when the background velocity model is incorrect, the use of this misfit function results in better focused migration images. Results suggest that our method best enhances image focusing when differences between predicted and observed data can be explained by traveltime shifts.

INTRODUCTION

Seismic migration can be described as the adjoint of a linearized forward-modeling operator applied to observed data (Claerbout, 1992). Migration produces a reflectivity image, an image of a perturbation to the background velocity model (Cohen and Bleistein, 1979), that approximates the true reflectivity insofar as the adjoint of the forward operator approximates the pseudoinverse. Typically, the adjoint is a poor approximation, and the accuracy of the computed reflectivity image can be significantly improved using the pseudoinverse of the forward operator rather than the adjoint. The use of the pseudoinverse of the forward operator in migration is known as least-squares migration (LSM) (Nemeth et al., 1999; Østmo and Plessix, 2002; Kühl and Sacchi, 2003; Plessix and Mulder, 2004; Dai, 2012).

LSM requires the inverse of the Hessian matrix (the normal operator) of second derivatives of a misfit function with respect to model parameters. The Hessian, however, is prohibitively expensive to compute and store for most practical-sized problems. Approximations of the inverse Hessian (Gray, 1997; Chavent and Plessix, 1999; Shin et al., 2001; Rickett, 2003; Guitton, 2004; Plessix and Mulder, 2004; Symes, 2008; Valenciano, 2008) are more feasible, and are often used to improve the quality of final migration images or to precondition iterative LSM. In this paper, we focus on iterative LSM, which can be used in conjunction with or in place of approximations of the Hessian. An advantage of iterative migration algorithms is that they typically are straightforward to implement; a disadvantage is that they can be more computationally expensive compared with an efficient approximation of the Hessian, or compared with a single application of the adjoint operator as is done, for example, in reverse-time migration (Baysal et al., 1983; Loewenthal and Mufti, 1983; McMechan, 1983; Whitmore, 1983; Levin, 1984).

The quality and accuracy of migration images depends greatly on the accuracy of the background velocity model, and errors in this background model can lead to an incoherent, defocused image. Ideally, the background velocity model should correctly predict the traveltimes of observed data, and should be sufficiently smooth so as not to generate reflected waves. These requirements derive from the conditions under which the Born approximation is valid (Symes, 2009), and under these conditions, migration can accurately image subsurface structures. However, when these conditions are violated, migration images are degraded and become defocused and incoherent. One reason for this degradation is that migration inverts for the perturbation to the background velocity model that controls only the amplitudes of predicted data; if the background model contains errors, then the predicted data will contain errors in traveltime and amplitude compared with the observed data, and both these types of errors — instead of only the amplitude errors — will contribute to the migration image.

Often, separating these types of errors, and perhaps discarding a certain type of error, can improve inversion results. For example, for full-waveform inversion (Tarantola, 1984; Pratt et al., 1998), authors advocate using only phase or traveltime information (Shin and Min,

Manuscript received by the Editor 7 October 2013; revised manuscript received 4 April 2014; published online 3 July 2014.

¹Colorado School of Mines, Golden, Colorado, USA. E-mail: sluo@mines.edu; dhale@mines.edu.

© 2014 Society of Exploration Geophysicists. All rights reserved.

2006; Bednar et al., 2007; Choi and Alkhalifah, 2011; Kamei et al., 2011), especially to update the low-wavenumber background model that is difficult for full-waveform inversion to recover from reflection seismic data (Snieder et al., 1989; Hicks and Pratt, 2001; Ma, 2012). Our task in LSM is complementary to that of full-waveform inversion for the background model. We seek to invert for the high-wavenumber component of the model, i.e., the perturbation to the background model. Thus, analogous to the use of phase or traveltime information to recover the low-wavenumber component of the velocity model, we propose to use amplitude information to recover the high-wavenumber component.

We propose a simple modification of the conventional least-squares misfit function used in iterative LSM. Rather than minimize the difference between predicted and observed data, we propose to minimize their difference after correcting for nonzero traveltime shifts. Assuming estimated traveltime shifts between predicted and observed data are accurate, this misfit function quantifies mostly amplitude differences. We demonstrate that the use of this amplitude misfit function in LSM results in more coherent and better focused images when the background velocity model used for migration differs from the true background velocity model.

METHODS

In this section, we first briefly review linearized waveform inversion and then discuss dynamic warping, the method we use to estimate traveltime shifts, before presenting our method for amplitude-only inversion.

Linearized waveform inversion

Wave propagation in the subsurface is described approximately by the constant-density acoustic-wave equation:

$$\sigma_0 \frac{\partial^2 u_0}{\partial t^2} - \Delta u_0 = f, \quad (1)$$

where u_0 is the wavefield, σ_0 is the squared background slowness, and f is the source function. Perturbing σ_0 by a scattering potential m and linearizing about m yields

$$\sigma_0 \frac{\partial^2 u}{\partial t^2} - \Delta u = -m \frac{\partial^2 u_0}{\partial t^2}, \quad (2)$$

where u is the scattered or perturbation wavefield. Often m is referred to as the reflectivity model or the reflectivity.

Let \mathbf{u}_s denote the discretized solution of equation 2 for a source function at position s . The wavefield \mathbf{u}_s is linear in the reflectivity \mathbf{m} :

$$\mathbf{u}_s = \mathbf{L}_s \mathbf{m}, \quad (3)$$

where \mathbf{L}_s is a linear prediction operator describing the evolution of the scattered wavefield in equation 2. The predicted data $\mathbf{p}_{s,r}$ are a subset of the wavefield \mathbf{u}_s :

$$\mathbf{p}_{s,r} = \mathbf{S}_r \mathbf{u}_s, \quad (4)$$

where \mathbf{S}_r is a sampling operator that extracts the wavefield at receiver position r .

To solve equation 4 for the reflectivity model \mathbf{m} , we minimize, in a least-squares sense, the difference between predicted data $\mathbf{p}_{s,r}$ and observed data $\mathbf{d}_{s,r}$:

$$\min_{\mathbf{m}} J(\mathbf{m}) = \sum_{s,r} E_{s,r}(\mathbf{u}_s(\mathbf{m})), \quad (5)$$

where

$$E_{s,r}(\mathbf{u}_s) = \frac{1}{2} \|\mathbf{S}_r \mathbf{u}_s - \mathbf{d}_{s,r}\|^2. \quad (6)$$

To minimize equation 5, we can pursue the negative of the gradient direction:

$$\frac{\partial J}{\partial \mathbf{m}} = \sum_{s,r} \mathbf{L}_s^T \left(\frac{\partial E_{s,r}}{\partial \mathbf{u}_s} \right), \quad (7)$$

where

$$\frac{\partial E_{s,r}}{\partial \mathbf{u}_s} = \mathbf{S}_r^T (\mathbf{S}_r \mathbf{u}_s - \mathbf{d}_{s,r}), \quad (8)$$

is the data residual. The adjoint of the prediction operator \mathbf{L}_s is a migration operator (Claerbout, 1992), and so we obtain the well-known result (Lailly, 1983; Tarantola, 1984) that the gradient of the least-squares misfit function can be computed by a migration of the residuals.

Dynamic warping

Before we can consider an amplitude misfit function, we require a method for estimating time-varying traveltimes between predicted and observed data. For this purpose, we use dynamic warping (Hale, 2013). Dynamic warping is robust and remains accurate in the presence of noise, and compared with more conventional methods for estimating traveltimes based on windowed cross-correlations, dynamic warping is more accurate, especially when traveltime shifts vary rapidly as a function of time (Hale, 2013).

Dynamic time warping (Sakoe and Chiba, 1978) is a method for computing integer time shifts $\tau = (\tau_1, \tau_2, \dots, \tau_n)$ between two sequences $\mathbf{p} = (p_1, p_2, \dots, p_n)$ and $\mathbf{d} = (d_1, d_2, \dots, d_n)$ such that

$$A = \frac{1}{2} \sum_i (p_i - d_{i+\tau_i})^2, \quad (9)$$

is minimized with respect to τ subject to the constraint:

$$|\tau_i - \tau_{i-1}| \leq 1/c, \quad (10)$$

where c is a positive integer. An attractive feature of dynamic time warping is that the algorithm is guaranteed to find the traveltime shifts τ that minimize equation 9 subject to constraint 10, and these shifts are such that $\partial A / \partial \tau = \mathbf{0}$ when the constraint is inactive.

Although we could use dynamic time warping to independently estimate traveltime shifts between all pairs of predicted and observed traces, in practice we find that using dynamic image warping (Hale, 2013) to estimate traveltime shifts between predicted and observed common shot gathers yields more accurate shifts, especially when predicted and observed data are not shifted versions of each

other (as is often the case even with synthetic data, and certainly always is the case with recorded field data). Dynamic image warping (Hale, 2013) approximately solves the extension to higher dimensions of the constrained optimization problem specified by equations 9 and 10, and in doing so, imposes constraints in time (equation 10) as well as in distance or offset on the estimated traveltime shifts.

Inversion of amplitude errors

To formulate an inversion of amplitude errors, we modify the observed data to include a time-shift operator:

$$\mathbf{b}_{s,r} = \mathbf{T}_{s,r} \mathbf{d}_{s,r}, \quad (11)$$

where $\mathbf{T}_{s,r}$ is a linear operator, e.g., a sinc interpolation operator, that shifts the observed data $\mathbf{d}_{s,r}$ by the traveltimes shifts $\tau_{s,r}$ estimated using dynamic warping. Note that $\mathbf{T}_{s,r}$ depends implicitly on the model \mathbf{m} because the traveltimes shifts $\tau_{s,r}$ are computed using the predicted data $\mathbf{p}_{s,r}$, which depend on the model.

The shifted observed data $\mathbf{b}_{s,r}$ can be viewed as a secondary data set obtained by processing the observed data. Processing of the observed data prior to migration is standard practice, even for conventional migration. The purpose of this processing is essentially to remove from the observed data any components that are due to an inconsistent model of wave propagation in the true subsurface. For example, just as an acoustic-wave equation cannot explain S-waves in elastic data, the linearized-wave equation (equation 2) with an incorrect background model cannot explain the traveltimes of the observed data. Migration using an incorrect background model is equivalent to migration using forward modeling that is inconsistent with the observed data, and so to properly migrate these data, we must first remove those components that cannot be explained by our forward modeling. Those components are the traveltimes.

Thus, we seek to minimize the difference between predicted data $\mathbf{p}_{s,r}$ and time-shifted observed data $\mathbf{b}_{s,r}$:

$$\min_{\mathbf{m}} J_A(\mathbf{m}) = \sum_{s,r} A_{s,r}(\mathbf{u}_s(\mathbf{m}), \tau_{s,r}(\mathbf{m})), \quad (12)$$

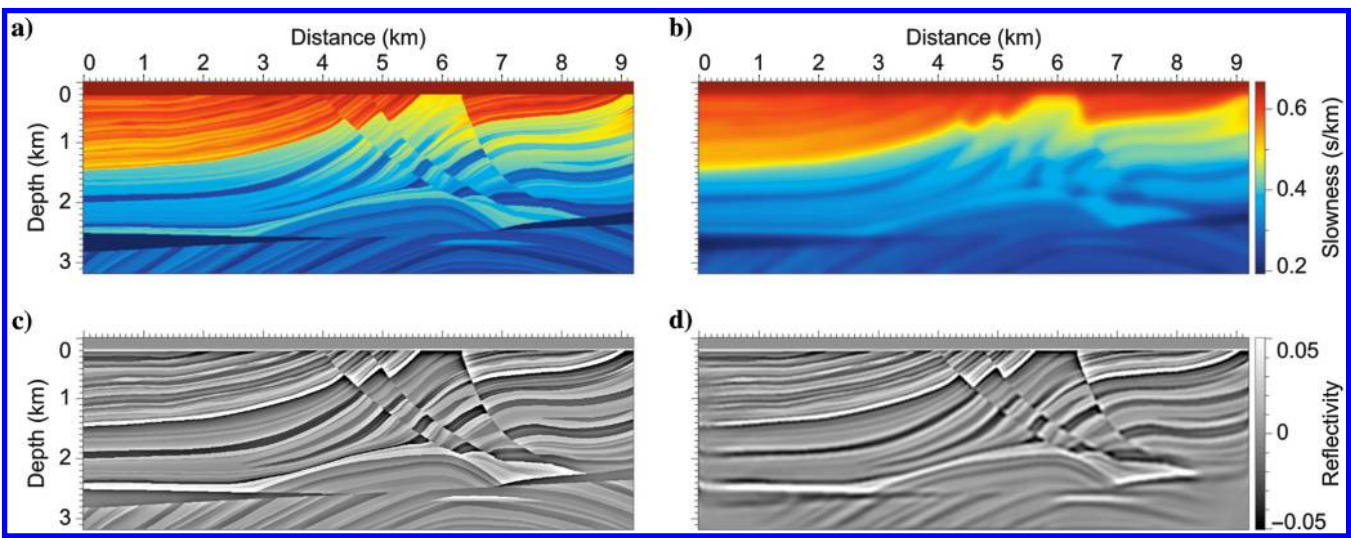


Figure 1. The (a) true slowness model, (b) true background slowness model, (c) true reflectivity computed as the difference between the true slowness squared and the true background slowness squared, and (d) LSM image.

where

$$A_{s,r} = \frac{1}{2} \|\mathbf{S}_r \mathbf{u}_s - \mathbf{T}_{s,r} \mathbf{d}_{s,r}\|^2. \quad (13)$$

Note that if the estimated traveltimes shifts $\tau_{s,r}$ are accurate, then equation 12 measures only amplitude errors between predicted and observed data. If the traveltimes shifts are zero, then equation 12 reduces to equation 5.

To minimize the misfit function in equation 12, we require its gradient with respect to model parameters:

$$\frac{\partial J_A}{\partial \mathbf{m}} = \sum_{s,r} \mathbf{L}_s^T \left(\frac{\partial A_{s,r}}{\partial \mathbf{u}_s} \right), \quad (14)$$

where

$$\frac{\partial A_{s,r}}{\partial \mathbf{u}_s} = \mathbf{S}_r^T (\mathbf{S}_r \mathbf{u}_s - \mathbf{T}_{s,r} \mathbf{d}_{s,r}). \quad (15)$$

Although $A_{s,r}$ depends on the estimated traveltimes shifts $\tau_{s,r}$, we need not consider this dependence when computing the residual in equation 15 because dynamic warping minimizes equation 13 (or equation 9) subject to constraint 10, so that $\partial A_{s,r} / \partial \tau_{s,r}$ is mostly zero. We refer to equation 15 as the amplitude residual and equation 12 as the amplitude misfit function, because they measure only amplitude errors between predicted and observed data.

RESULTS

We compare conventional LSM with the proposed method of least-squares migration of amplitude errors (LSMA) on a 2D synthetic data set, and on a 2D field data set.

For LSM, the data are linear in the reflectivity, and thus LSM images can be computed by minimizing equation 5 with (linear) conjugate gradient iterations. To compute LSMA images by solving equation 12, however, is a nonlinear problem because the reflectivity \mathbf{m} depends on the traveltimes shifts $\tau_{s,r}$, but the traveltimes shifts

also depend on the reflectivity. We can compute LSMA images either by minimizing equation 12 using a gradient-based descent method (e.g., steepest descent or nonlinear conjugate gradient), or alternatively, by first solving equation 12 with fixed traveltime shifts $\tau_{s,r}$, then recomputing the traveltime shifts and solving equation 12 with the new shifts, repeating until convergence.

Note that when the traveltime shifts $\tau_{s,r}$ are zero, equation 12 is equivalent to equation 5. This is the case for the first nonlinear iteration or the first solution of equation 12 with fixed $\tau_{s,r}$, in which the

reflectivity is zero and hence the traveltime shifts are zero. After the first nonlinear iteration or the first solution of equation 12, we obtain a nonzero reflectivity image from which to predict data and to estimate possibly nonzero traveltime shifts.

Synthetic data example

The background slowness used for modeling and migration is shown in Figure 1b, and is computed by smoothing a modified

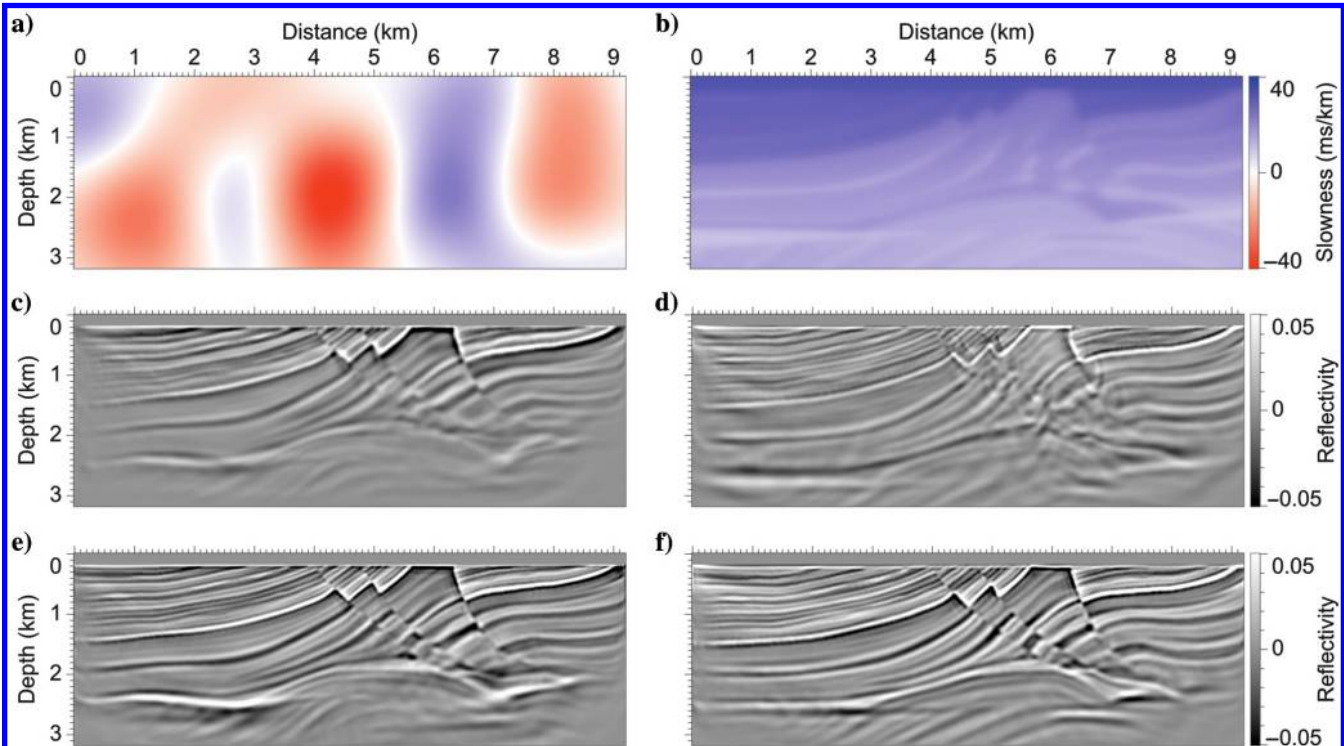


Figure 2. The (a and b) difference between the true background slowness shown in Figure 1b and the background slowness used for migration; (c) LSM image computed for the background slowness with error shown in (a); (d) LSM image computed for the background slowness with error shown in (b); (e) LSMA image computed for the background slowness with error shown in (a); (f) LSMA image computed for the background slowness with error shown in (b).

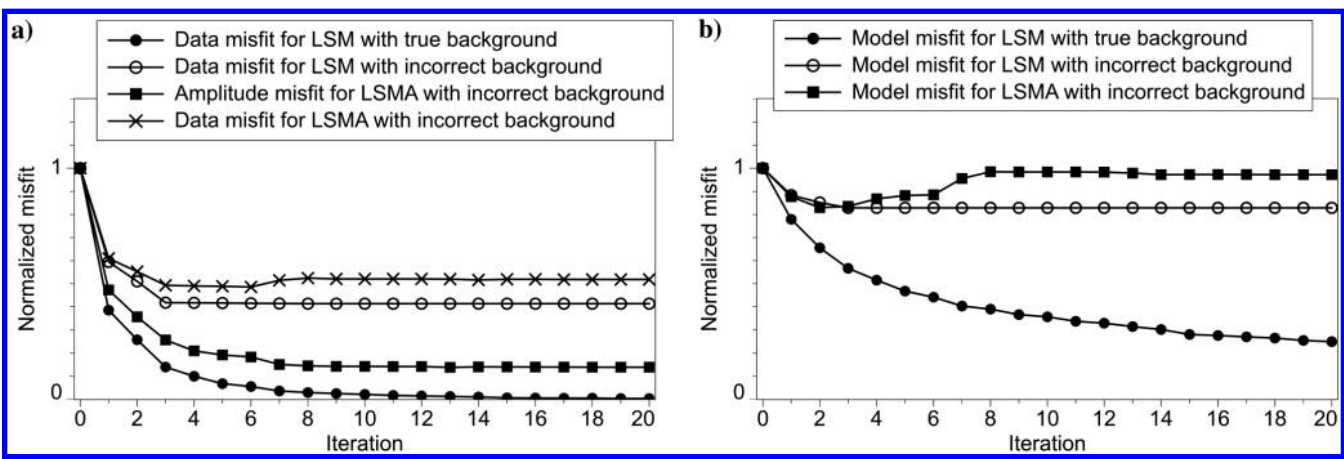


Figure 3. Normalized (a) data and amplitude misfit and (b) model misfit for LSM and LSMA. Here, *true background* refers to the true background slowness shown in Figure 1b, whereas *incorrect background* refers to the background slowness with error shown in Figure 2a.

Marmousi model (Lailly and Versteeg, 1990) shown in Figure 1a along the depth and distance axes using a two-sided exponential filter with 100-m width. The true reflectivity shown in Figure 1c is then computed as the difference between the true slowness (Figure 1a) squared and the true background slowness (Figure 1b) squared. Using the true background slowness and true reflectivity, we simulate observed data by solving equations 1 and 2 for a Ricker source function with peak frequency 10 Hz. To facilitate comparison of LSM and LSMA, all migration images for these synthetic data are computed using 20 nonlinear conjugate gradient iterations. Hence, because the cost of dynamic warping is small compared with the cost of modeling and migration, the LSM and LSMA images computed for these synthetic data come at comparable costs.

The first example shown in Figure 1 demonstrates conventional LSM using the true background slowness for migration. The reflectivity image shown in Figure 1d is obtained after 20 nonlinear conjugate gradient iterations (Nocedal and Wright, 2000) of LSM using the true background slowness with 153 shots and 767 receivers evenly spaced along the surface. As expected, this computed reflectivity matches well the true reflectivity shown in Figure 1c because the background slowness model used for migration was exactly the true background slowness. In practice, we expect the background slowness model used to migrate the data to differ from the true background slowness model.

Figure 2 illustrates the effects of erroneous background slowness models on the reflectivity images obtained using LSM and LSMA. Figure 2a and 2b shows the differences between the true background slowness model (Figure 1b) and the background slowness models that we use for migration. The slowness error shown in Figure 2a was computed by smoothing a random slowness model, whereas the error shown in Figure 2b resulted from scaling the true background slowness by 95%.

Figure 2c and 2d shows the reflectivity images computed using 20 iterations of LSM with the erroneous background slowness models with errors shown in Figure 2a and 2b, respectively. Compared with the reflectivity image (Figure 1d) computed using the true background slowness, the image in Figure 2c is degraded, and shows uneven illumination and defocused reflectors, especially at greater depths where traveltimes errors resulting from the erroneous background slowness are more severe. This degradation is also seen

in the reflectivity image shown in Figure 2d. The quality of this image is worse than the image shown in Figure 2c because the slowness errors (Figure 2b) all have the same sign, and so traveltimes errors in the predicted data accumulate more quickly than traveltimes errors for data predicted with the slowness model with error shown in Figure 2a.

Figure 2e and 2f shows the reflectivity images computed with 20 iterations of LSMA. Compared with the conventional LSM images (Figure 2c and 2d), the LSMA images show improved illumination of deeper portions of the model, and better focused and more continuous reflectors throughout. Note, however, that the positions of features in LSMA images (Figure 2e and 2f) are shifted compared

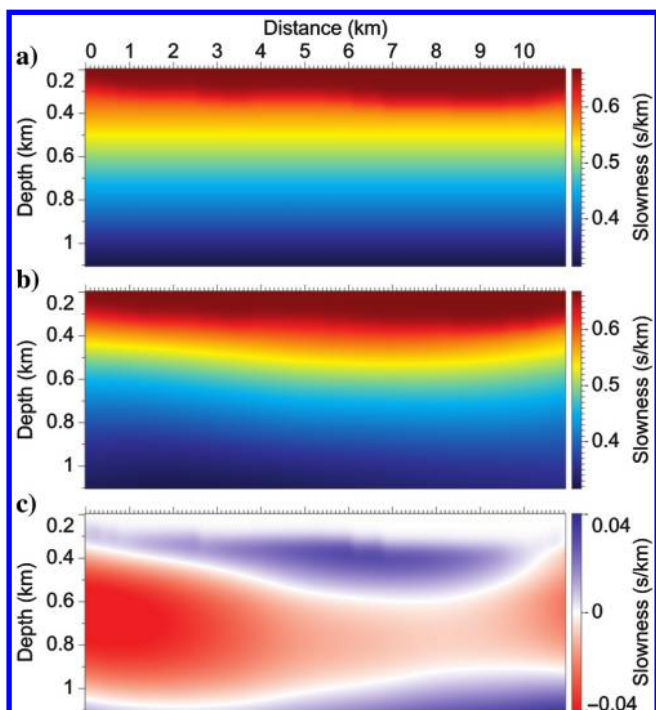


Figure 5. The (a) laterally invariant slowness model, (b) optimized slowness model, and the (c) difference between (b) and (a).

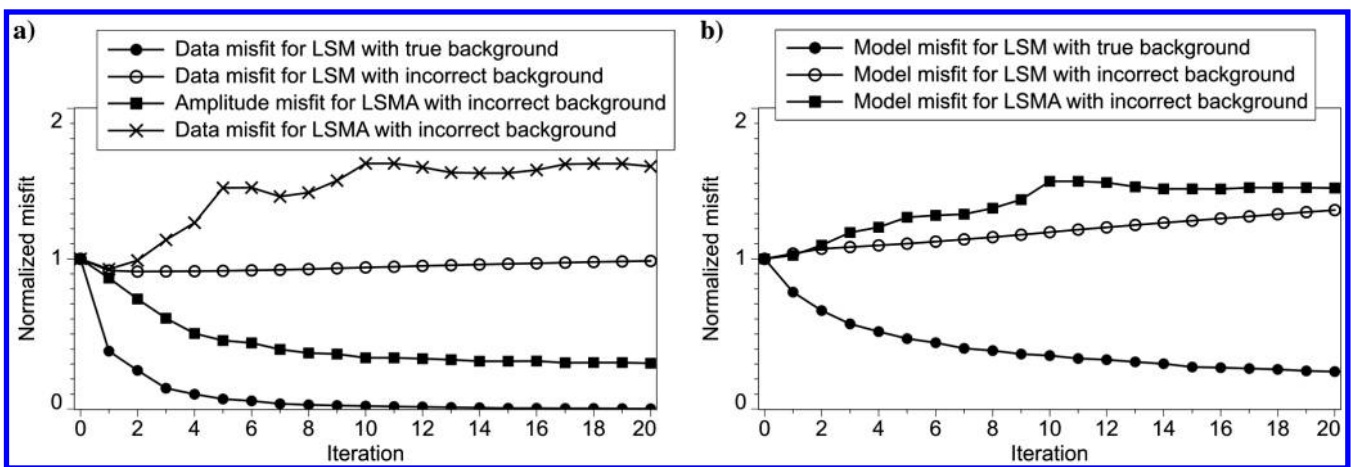


Figure 4. Normalized (a) data and amplitude misfit and (b) model misfit for LSM and LSMA. Here, true background refers to the true background slowness shown in Figure 1b, whereas incorrect background refers to the background slowness with error shown in Figure 2b.

with their positions in the true reflectivity (Figure 1c). This mispositioning is expected, however, because LSMA images are computed using erroneous background slowness models.

The presence of remaining traveltime shifts between predicted and observed data, as well as spatial shifts between image features in computed LSMA images and those in the true reflectivity, is confirmed by the misfit functions shown in Figures 3 and 4. Figures 3a and 4a show normalized data and amplitude misfit functions, whereas Figures 3b and 4b show normalized model misfit functions (the L^2 -norm of the difference between the computed reflectivity and the true reflectivity) for LSM and LSMA images computed using either the true background slowness model shown in Figure 1b or the erroneous background slowness model with error shown in Figure 2a or Figure 2b. In Figures 3a and 4a, note that the data misfit is not used in LSMA, but more importantly, notice that the data misfit increases in iteration 7 in Figure 3a and in iteration 2 in Figure 4a. This indicates that the better-focused LSMA images shown in Figure 2e and 2f cannot be obtained with conventional LSM, which minimizes the data misfit.

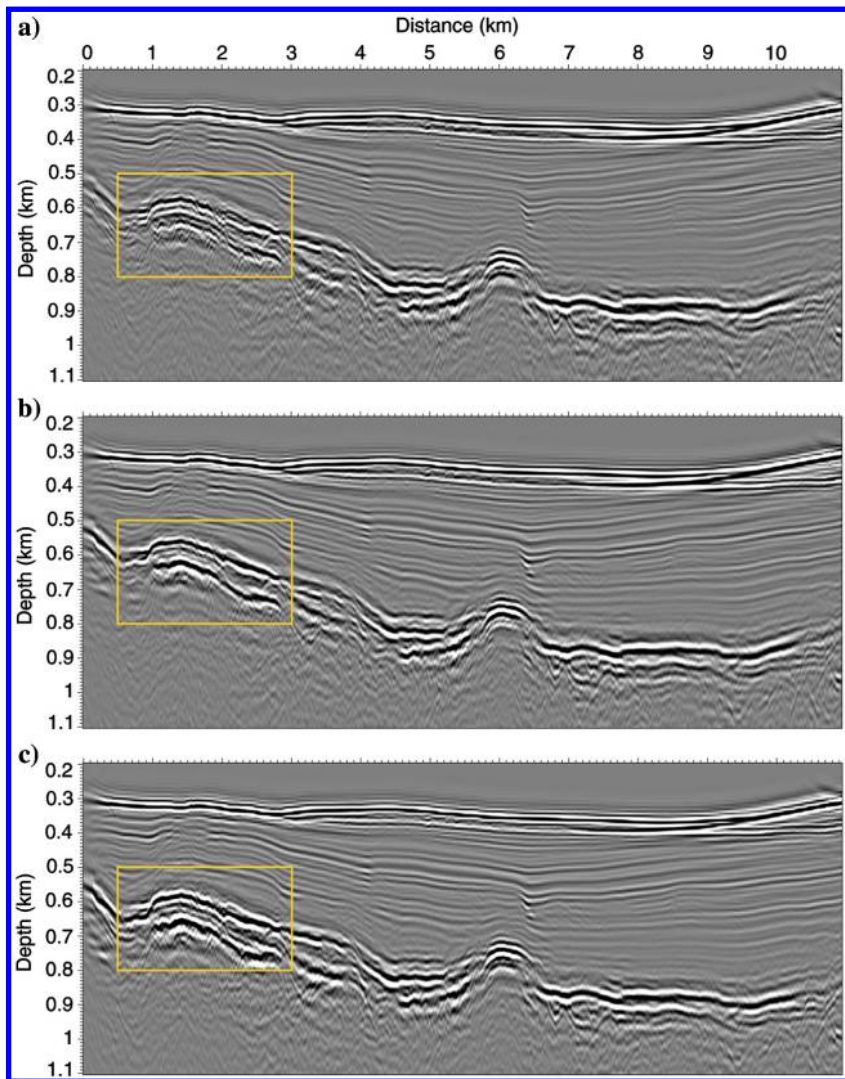
The model misfits shown in Figures 3b and 4b indicate that, for the erroneous background slowness models shown in Figure 2a and

2b, the LSM images (Figure 2c and 2d) more closely match the true reflectivity (Figure 1c) than do the LSMA images (Figure 2e and 2f). Indeed, a zero-reflectivity image is closer to the true reflectivity than the LSMA image shown in Figure 2f. However, the large model misfits for LSMA images reflect the fact that features in these images are shifted relative to the corresponding features in the true reflectivity. Although image features in LSMA images are shifted, it is clear that the amplitudes (but not the positions) of these features better match those of the true reflectivity.

Field data example

Next, we test our method for amplitude-only migration on a subset of a field data set provided by Eni E&P. The entire 2D data set contains 3661 shots with a shot spacing of 12.5 m, and was recorded using a streamer with 99 receivers with a receiver spacing of 12.5 m and maximum offset of 1.225 km. The subset of the data that we migrate consists of 431 shots with shot spacing of 25 m. The data have been regularized, and multiples have been attenuated. We estimate a zero-phase wavelet from the amplitude spectrum computed from a subset of the recorded data (Claerbout, 1992),

Figure 6. The (a) LSM image, (b) LSMA image computed for the laterally invariant slowness model shown in Figure 5a, and (c) the LSM image computed for the optimized slowness model shown in Figure 5b.



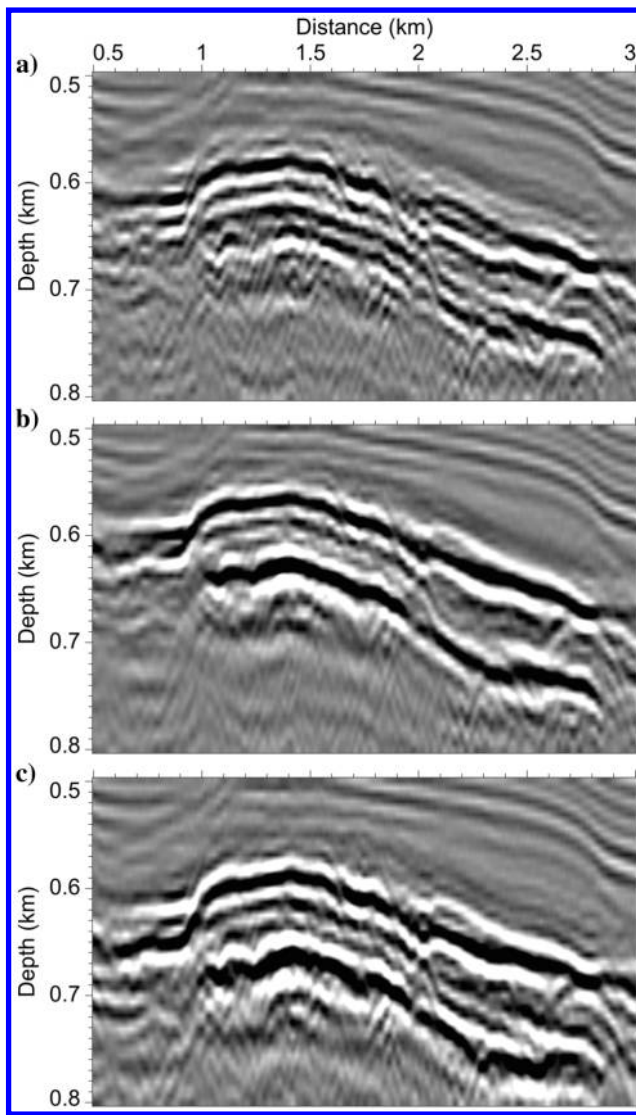


Figure 7. Zoomed views of the areas enclosed by yellow boxes in (a) Figure 6a, (b) Figure 6b, and (c) Figure 6c.

and we apply a band-pass filter to the estimated wavelet and the recorded data to remove frequency content below 20 Hz and greater than 80 Hz prior to migration.

We compare LSM and LSMA for two slowness models. The first slowness model, shown in Figure 5a, is laterally invariant (except near the sea floor), whereas the second, shown in Figure 5b, is an optimized slowness model that was provided with the recorded data. The LSM and LSMA images computed for the laterally invariant slowness model (Figure 5a) are shown in Figure 6a and 6b, respectively. Comparing these images, we observe that reflectors in the LSMA image are more continuous and better focused than corresponding reflectors in the LSM image. Moreover, image features in the LSMA image (Figure 6b) are similar to features seen in the LSM image (Figure 6c) computed for the optimized slowness model (Figure 5b), despite the use of a much simpler slowness model for LSMA. Differences between the migration images shown in Figure 6a and 6b are most apparent in the areas enclosed by yellow boxes, in which the slowness differences (Figure 5c) between the models used for migration are relatively large. Zoomed views of the areas enclosed by yellow boxes in Figure 6a, 6b, and 6c are shown in Figure 7a, 7b, and 7c, respectively. Elsewhere, where slowness errors are smaller, differences between the migration images are less significant, as one would expect.

It is worth noting that, for this example, it was necessary to use 3D dynamic warping in LSMA. For 3D warping, rather than independently warp predicted to observed shot gathers as was done for the synthetic examples shown in Figure 2, we instead warped simultaneously all predicted shot gathers to all observed shot gathers, at each iteration of LSMA. A 3D warping enables us to constrain changes in estimated traveltimes with shot location, which results in more accurate shifts. For synthetic tests, in which the same forward modeling code is used to simulate predicted and observed data, this additional constraint is perhaps unnecessary. For field data, however, an additional constraint on the traveltimes shifts can significantly improve the accuracy of estimated shifts, especially in cases where the data quality is low.

Because we compute LSMA images by minimizing the difference between predicted and shifted observed data (equation 12), the predicted data in general will not have the same traveltimes

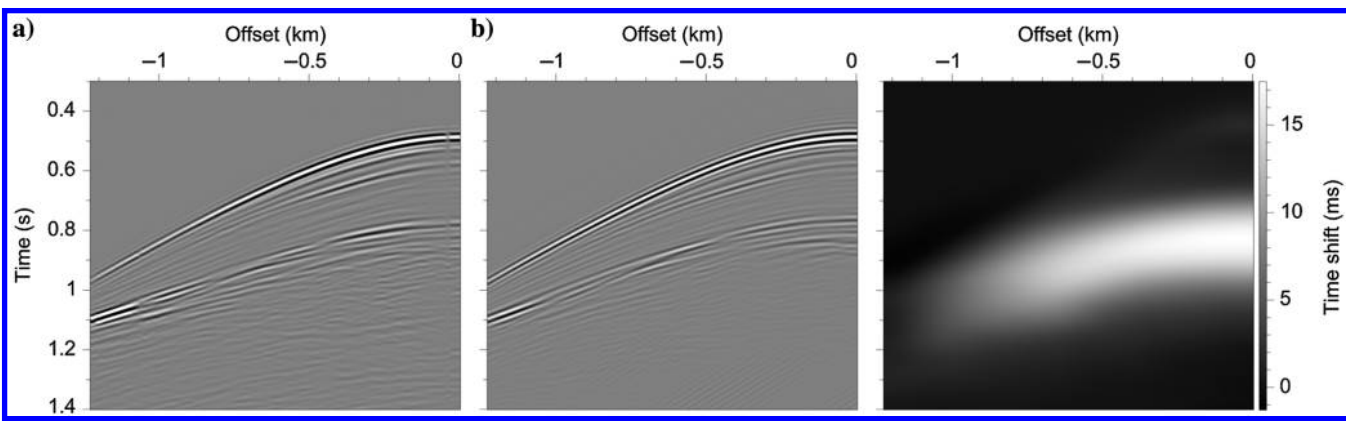


Figure 8. For the shot located at distance 1.85 km, the (a) observed data, (b) predicted data computed using the laterally invariant slowness model shown in Figure 5a and the LSMA image shown in Figure 6b, and (c) traveltime shifts between (a) and (b).

as the original observed data. An example of these traveltime differences for data corresponding to the shot located at distance 1.85 km is shown in Figure 8. Figure 8a shows the observed data, Figure 8b shows the predicted data computed using the laterally invariant slowness model (Figure 5a) and the LSMA image (Figure 6b), and Figure 8c shows the traveltime shifts between the data shown in Figure 8a and 8b. The remaining traveltime shifts seen in Figure 8c exceed one half period, which confirms that LSMA yields an image that explains the dynamics, but not the kinematics, of the observed data.

DISCUSSION

The improvement in LSMA images compared with conventional LSM images depends on the nature of the background slowness error, and also on the acquisition geometry. A comparison between the images shown in Figure 2e and 2f suggests that LSMA provides a greater improvement in image quality and reflector focusing for small, systematic errors in background slowness (e.g., Figure 2b), perhaps because, in such situations, traveltime shifts can well explain the differences between predicted and observed data. When the background slowness error is more complex or is too large, predicted and observed data might be inconsistent, i.e., events in one data set do not have corresponding events in the other, making it difficult to estimate accurate shifts; or, predicted and observed data might differ by significant horizontal spatial shifts in addition to vertical traveltime shifts, in which case estimating only traveltime shifts for use in LSMA might be inadequate. Although dynamic warping can also be used to estimate horizontal shifts, only vertical traveltime shifts were used in the examples shown above.

The improvement in LSMA images also depends on acquisition geometry. Traveltime differences between observed and predicted data in LSM arise from errors in the background slowness model used for migration, but more specifically, they arise from inconsistencies between different images of the same subsurface geologic structures, e.g., images computed for neighboring individual shots. Thus, we expect LSMA to provide greater improvement over conventional LSM when the recorded data provide redundant information about subsurface geologic structures. Conversely, we expect LSMA and LSM images to be more similar when data provide independent information, for example, when shots are sparsely located or shot spacing is large, or when the maximum source-receiver offset or the offset-to-depth ratio is small.

Although LSMA images can provide an improved estimate of the amplitudes of the true reflectivity, ultimately, we seek a complete model of the subsurface, which includes not only an accurate reflectivity model but also an accurate background slowness model. The proposed method could potentially be extended and used to aid an inversion for the background slowness. A simple approach might be to hold the reflectivity model constant following LSMA, and then invert the remaining traveltime shifts between predicted and observed data to update the background slowness.

Finally, it is perhaps worth mentioning that a method similar to LSMA can be formulated by introducing a time-shift operator $\mathbf{T}_{s,r}^{-1}$ to the right side of equation 4, to be applied after computing the predicted data. The resulting forward modeling equation, in which the time-shift operator can be considered a residual modeling operator, leads to an inversion scheme similar to LSMA, the main difference being that the predicted data rather than the observed data are

shifted in the computation of the gradient. The resulting image, however, in general differs from the LSMA image (in fact, they are equivalent only in the case of constant shifts). We tested this alternate method on the examples shown above, but the results we obtained were inferior, i.e., image features were less similar to features in the image computed using the best available slowness model, to those obtained with LSMA.

CONCLUSION

We have presented a method for LSM that minimizes an amplitude misfit function defined with differences between predicted data and shifted observed data, with traveltime shifts between predicted and observed data estimated using dynamic warping. The use of this amplitude misfit function results in a more coherent and better focused migration image when the background slowness model used for migration contains errors. These LSMA images contain image features with amplitudes that match those of the true reflectivity, but with positions that are shifted relative to the positions of corresponding features in the true reflectivity. Thus, LSMA images are perhaps better suited for interpretation of geologic structures, but to correctly position interpreted structures, we would need to first correctly position LSMA image features. One way to correct for the mispositioning of image features is to first align the features with measurements of subsurface properties obtained from well logs and then interpolate alignment shifts between well-log locations to generate shifts for an entire image.

ACKNOWLEDGMENTS

This work was supported by the sponsors of the Consortium Project on Seismic Inverse Methods for Complex Structures at the Colorado School of Mines. We thank C. Fleury for helpful discussions and for sharing his insights on this problem. Thanks also go to I. Vasconcelos and three anonymous reviewers whose comments and suggestions helped to improve the manuscript. The field data were provided courtesy of Eni E&P.

REFERENCES

- Baysal, E., D. Kosloff, and J. Sherwood, 1983, Reverse time migration: Geophysics, **48**, 1514–1524, doi: [10.1190/1.1441434](https://doi.org/10.1190/1.1441434).
- Bednar, J. B., C. Shin, and S. Pyun, 2007, Comparison of waveform inversion, Part 2: Phase approach: Geophysical Prospecting, **55**, 465–475, doi: [10.1111/j.1365-2478.2007.00618.x](https://doi.org/10.1111/j.1365-2478.2007.00618.x).
- Chavent, G., and R. Plessix, 1999, An optimal true-amplitude least-squares prestack depth-migration operator: Geophysics, **64**, 508–515, doi: [10.1190/1.1444557](https://doi.org/10.1190/1.1444557).
- Choi, Y., and T. Alkhalifah, 2011, Frequency-domain waveform inversion using the unwrapped phase: 81st Annual International Meeting, SEG, Expanded Abstracts, 2576–2580.
- Claerbout, J. F., 1992, Earth soundings analysis: Processing versus inversion: Blackwell Scientific Publications.
- Cohen, J. K., and N. Bleistein, 1979, Velocity inversion procedure for acoustic waves: Geophysics, **44**, 1077–1087, doi: [10.1190/1.1440996](https://doi.org/10.1190/1.1440996).
- Dai, W., 2012, Multisource least-squares reverse time migration: Ph.D. thesis, King Abdullah University of Science and Technology.
- Gray, S., 1997, True amplitude migration: A comparison of three approaches: Geophysics, **62**, 929–936, doi: [10.1190/1.1444200](https://doi.org/10.1190/1.1444200).
- Guitton, A., 2004, Amplitude and kinematic corrections of migrated images for nonunitary imaging operators: Geophysics, **69**, 1017–1024, doi: [10.1190/1.1778244](https://doi.org/10.1190/1.1778244).
- Hale, D., 2013, Dynamic warping of seismic images: Geophysics, **78**, no. 2, S105–S115, doi: [10.1190/geo2012-0327.1](https://doi.org/10.1190/geo2012-0327.1).
- Hicks, G., and R. Pratt, 2001, Reflection waveform inversion using local descent methods: Estimating attenuation and velocity over a gas-sand deposit: Geophysics, **66**, 598–612, doi: [10.1190/1.1444951](https://doi.org/10.1190/1.1444951).

- Kamei, R., A. J. Brenders, and R. G. Pratt, 2011, A discussion on the advantages of phase-only waveform inversion in the Laplace-Fourier domain: Validation with marine and land seismic data: 81st Annual International Meeting, SEG, Expanded Abstracts, 2476–2481.
- Kühl, H., and M. D. Sacchi, 2003, Least-squares wave-equation migration for AVP/AVA inversion: *Geophysics*, **68**, 262–273, doi: [10.1190/1.1543212](https://doi.org/10.1190/1.1543212).
- Lailly, P., 1983, The seismic inverse problem as a sequence of before stack migration: *in*, J. B. Bednar, E. Robinson, and A. Weglein, eds., Conference on Inverse Scattering: Theory and Application, SIAM, 206–220.
- Lailly, P., and R. Versteeg, 1990, The Marmousi workshop — Introduction: Presented at 52nd EAEG Workshop, Practical Aspects of Seismic Data Inversion.
- Levin, S., 1984, Principle of reverse-time migration: *Geophysics*, **49**, 581–583, doi: [10.1190/1.1441693](https://doi.org/10.1190/1.1441693).
- Loewenthal, D., and I. Mufti, 1983, Reversed time migration in spatial frequency domain: *Geophysics*, **48**, 627–635, doi: [10.1190/1.1441493](https://doi.org/10.1190/1.1441493).
- Ma, Y., 2012, Waveform-based velocity estimation from reflection seismic data: Ph.D. thesis, Colorado School of Mines.
- McMechan, G. A., 1983, Migration by extrapolation of time-dependent boundary values: *Geophysical Prospecting*, **31**, 413–420, doi: [10.1111/j.1365-2478.1983.tb01060.x](https://doi.org/10.1111/j.1365-2478.1983.tb01060.x).
- Nemeth, T., C. Wu, and G. T. Schuster, 1999, Least-squares migration of incomplete reflection data: *Geophysics*, **64**, 208–221, doi: [10.1190/1.1444517](https://doi.org/10.1190/1.1444517).
- Nocedal, J., and S. J. Wright, 2000, Numerical optimization: Springer Science + Business Media, LLC.
- Østmo, S., and R.-E. Plessix, 2002, Finite-difference iterative migration by linearized waveform inversion in the frequency domain: 72nd Annual International Meeting, SEG, Expanded Abstracts, 1384–1387.
- Plessix, R.-E., and W. A. Mulder, 2004, Frequency-domain finite-difference amplitude-preserving migration: *Geophysical Journal International*, **157**, 975–987, doi: [10.1111/j.1365-246X.2004.02282.x](https://doi.org/10.1111/j.1365-246X.2004.02282.x).
- Pratt, R. G., C. Shin, and G. Hicks, 1998, Gauss–Newton and full Newton methods in frequency-space seismic waveform inversion: *Geophysical Journal International*, **133**, 341–362, doi: [10.1046/j.1365-246X.1998.00498.x](https://doi.org/10.1046/j.1365-246X.1998.00498.x).
- Rickett, J. E., 2003, Illumination-based normalization for wave-equation depth migration: *Geophysics*, **68**, 1371–1379, doi: [10.1190/1.1598130](https://doi.org/10.1190/1.1598130).
- Sakoe, H., and S. Chiba, 1978, Dynamic programming algorithm optimization for spoken word recognition: *IEEE Transactions on Acoustics, Speech, and Signal Processing*, **26**, 43–49, doi: [10.1109/TASSP.1978.1163055](https://doi.org/10.1109/TASSP.1978.1163055).
- Shin, C., S. Jang, and D. J. Min, 2001, Improved amplitude preservation for prestack depth migration by inverse scattering theory: *Geophysical Prospecting*, **49**, 592–606, doi: [10.1046/j.1365-2478.2001.00279.x](https://doi.org/10.1046/j.1365-2478.2001.00279.x).
- Shin, C., and D. J. Min, 2006, Waveform inversion using a logarithmic wavefield: *Geophysics*, **71**, no. 3, R31–R42, doi: [10.1190/1.2194523](https://doi.org/10.1190/1.2194523).
- Snieder, R., M. Xie, A. Pica, and A. Tarantola, 1989, Retrieving both the impedance contrast and background velocity: A global strategy for the seismic reflection problem: *Geophysics*, **54**, 991–1000, doi: [10.1190/1.1442742](https://doi.org/10.1190/1.1442742).
- Symes, W. W., 2008, Approximate linearized inversion by optimal scaling of prestack depth migration: *Geophysics*, **73**, no. 2, R23–R35, doi: [10.1190/1.2836323](https://doi.org/10.1190/1.2836323).
- Symes, W. W., 2009, The seismic reflection inverse problem: *Inverse Problems*, **25**, 1–39, doi: [10.1088/0266-5611/25/12/123008](https://doi.org/10.1088/0266-5611/25/12/123008).
- Tarantola, A., 1984, Inversion of seismic reflection data in the acoustic approximation: *Geophysics*, **49**, 1259–1266, doi: [10.1190/1.1441754](https://doi.org/10.1190/1.1441754).
- Valenciano, A., 2008, Imaging by wave-equation inversion: Ph.D. thesis, Stanford University.
- Whitmore, N. D., 1983, Iterative depth migration by backward time propagation: 53rd Annual International Meeting, SEG, Expanded Abstracts, 382–385.

This article has been cited by:

1. Yanbao Zhang, Yike Liu, Jia Yi. 2022. Least-Squares Reverse-Time Migration of Water-Bottom-Related Multiples. *Remote Sensing* **14**:23, 5979. [[Crossref](#)]
2. Jidong Yang, Jianping Huang, Jie Xu, Yang Zhao. 2022. Quantitative Error Analysis for the Least-Squares Imaging. *IEEE Transactions on Geoscience and Remote Sensing* **60**, 1-10. [[Crossref](#)]
3. A. Maul, A. Bulcão, R.M. Dias, B. Pereira-Dias, L. Teixeira, F. Borges, M. González, C. Guizan, M. Cetale. 2021. Benefits of inserting salt stratification to detail velocity model prior to least-squares reverse-time migration. *Journal of Applied Geophysics* **195**, 104469. [[Crossref](#)]
4. Yan-Bao Zhang, Yi-Ke Liu, Jia Yi, Xue-Jian Liu. 2021. First-order multiples imaging aided by water bottom. *Petroleum Science* **18**:6, 1650-1661. [[Crossref](#)]
5. Carlos Alberto da Costa Filho, Gregório Goudel Azevedo, Roberto Pereira, Adel Khalil. 2021. Efficient iterative prestack least-squares reverse time migration through surface-offset gather compression. *GEOPHYSICS* **86**:6, S417-S430. [[Abstract](#)] [[Full Text](#)] [[PDF](#)] [[PDF w/Links](#)]
6. Ram Tuvi, Zeyu Zhao, Mrinal K Sen. 2021. A fast least-squares migration with ultra-wide-band phase-space beam summation method. *Journal of Physics Communications* **5**:10, 105013. [[Crossref](#)]
7. Meixia Wang, Sheng Xu, Hongbo Zhou, Bing Tang, Aaron DeNosaquo, Gentiana Ionescu, Graeme Douglas Mackenzie. Efficient least-squares reverse time migration with common-shot gathers 2913-2917. [[Abstract](#)] [[Enhanced Abstract](#)] [[PDF](#)] [[PDF w/Links](#)]
8. Toktam Zand, Hamid R. Siahkoohi, Alison Malcolm, Ali Gholami, Alan Richardson. 2020. Consensus optimization of total variation-based reverse time migration. *Computational Geosciences* **24**:3, 1393-1407. [[Crossref](#)]
9. Bin He, Yike Liu. 2020. Wave-Equation Migration Velocity Analysis Using Radon-Domain Common-Image Gathers. *Journal of Geophysical Research: Solid Earth* **125**:2. . [[Crossref](#)]
10. Yanbao Zhang, Yike Liu, Xuejian Liu, Xiaopeng Zhou. 2020. Reverse time migration using water-bottom-related multiples. *Geophysical Prospecting* **68**:2, 446-465. [[Crossref](#)]
11. Bin He, Yike Liu, Yanbao Zhang. 2019. Improving the least-squares image by using angle information to avoid cycle skipping. *GEOPHYSICS* **84**:6, S581-S598. [[Abstract](#)] [[Full Text](#)] [[PDF](#)] [[PDF w/Links](#)]
12. Jizhong Yang, Yunyue Elita Li, Arthur Cheng, Yuzhu Liu, Liangguo Dong. 2019. Least-squares reverse time migration in the presence of velocity errors. *GEOPHYSICS* **84**:6, S567-S580. [[Abstract](#)] [[Full Text](#)] [[PDF](#)] [[PDF w/Links](#)]
13. Zeyu Zhao, Mrinal K. Sen. 2019. Frequency-domain double-plane-wave least-squares reverse time migration. *Geophysical Prospecting* **67**:8, 2061-2084. [[Crossref](#)]
14. Chuang Li, Jianping Huang, Zhenchun Li, Han Yu, Rongrong Wang. 2019. Least-squares migration with primary- and multiple-guided weighting matrices. *GEOPHYSICS* **84**:3, S171-S185. [[Abstract](#)] [[Full Text](#)] [[PDF](#)] [[PDF w/Links](#)]
15. Qingchen Zhang, Weijian Mao, Yangkang Chen. 2019. Attenuating Crosstalk Noise of Simultaneous-Source Least-Squares Reverse Time Migration With GPU-Based Excitation Amplitude Imaging Condition. *IEEE Transactions on Geoscience and Remote Sensing* **57**:1, 587-597. [[Crossref](#)]
16. Wei Dai, Xin Cheng, Kun Jiao, Denes Vigh. Least-squares reverse time migration with dynamic time warping 4241-4245. [[Abstract](#)] [[Enhanced Abstract](#)] [[PDF](#)] [[PDF w/Links](#)] [[Supplementary Material](#)]
17. Jizhong Yang, Yunyue Elita Li, Arthur Cheng, Yuzhu Liu, Liangguo Dong. Least-squares reverse time migration with velocity errors 4256-4260. [[Abstract](#)] [[Enhanced Abstract](#)] [[PDF](#)] [[PDF w/Links](#)] [[Supplementary Material](#)]
18. Peng Guo, George A. McMechan. 2018. Compensating Q effects in viscoelastic media by adjoint-based least-squares reverse time migration. *GEOPHYSICS* **83**:2, S151-S172. [[Abstract](#)] [[Full Text](#)] [[PDF](#)] [[PDF w/Links](#)]
19. Hao Zhang, Qiancheng Liu, Jizhong Wu. 2017. Improving imaging quality using least-squares reverse time migration: application to data from Bohai basin. *Journal of Geophysics and Engineering* **14**:5, 1315-1326. [[Crossref](#)]
20. Chong Zeng, Shuqian Dong, Bin Wang. 2017. A guide to least-squares reverse time migration for subsalt imaging: Challenges and solutions. *Interpretation* **5**:3, SN1-SN11. [[Abstract](#)] [[Full Text](#)] [[PDF](#)] [[PDF w/Links](#)]
21. Tong Bai, Ilya Tsvankin, Ximeng Wu. Waveform inversion of synthetic reflection data for VTI attenuation parameters 431-436. [[Abstract](#)] [[Enhanced Abstract](#)] [[PDF](#)] [[PDF w/Links](#)] [[Supplementary Material](#)]
22. Meixia Wang, Sheng Xu. Least-squares reverse time migration with inaccurate velocity model 4405-4410. [[Abstract](#)] [[Enhanced Abstract](#)] [[PDF](#)] [[PDF w/Links](#)]

- 23.. Anistropy Complete Session 279-476. [[Abstract](#)] [[PDF](#)] [[PDF w/Links](#)]
- 24.. Seismic Processing: Migration I Complete Session 4353-4560. [[Abstract](#)] [[PDF](#)] [[PDF w/Links](#)]
25. Tong Bai, Ilya Tsvankin, Xinming Wu. 2017. Waveform inversion for attenuation estimation in anisotropic media. *GEOPHYSICS* 82:4, WA83-WA93. [[Abstract](#)] [[Full Text](#)] [[PDF](#)] [[PDF w/Links](#)]
26. Xuejian Liu, Yike Liu, Huiyi Lu, Hao Hu, Majid Khan. 2017. Prestack correlative least-squares reverse time migration. *GEOPHYSICS* 82:2, S159-S172. [[Abstract](#)] [[Full Text](#)] [[PDF](#)] [[PDF w/Links](#)]
27. Gaurav Dutta. 2017. Sparse least-squares reverse time migration using seislets. *Journal of Applied Geophysics* 136, 142-155. [[Crossref](#)]
28. Jizhong Yang, Yuzhu Liu, Liangguo Dong. 2016. Least-squares reverse time migration in the presence of density variations. *GEOPHYSICS* 81:6, S497-S509. [[Abstract](#)] [[Full Text](#)] [[PDF](#)] [[PDF w/Links](#)]
29. Qingchen Zhang, Hui Zhou, Hanming Chen, Jie Wang. 2016. Least-squares reverse time migration with and without source wavelet estimation. *Journal of Applied Geophysics* 134, 1-10. [[Crossref](#)]
30. Yike Liu, Xuejian Liu, Are Osen, Yu Shao, Hao Hu, Yingcai Zheng. 2016. Least-squares reverse time migration using controlled-order multiple reflections. *GEOPHYSICS* 81:5, S347-S357. [[Abstract](#)] [[Full Text](#)] [[PDF](#)] [[PDF w/Links](#)]
31. Yin Huang, Rami Nammour, William Symes. 2016. Flexibly preconditioned extended least-squares migration in shot-record domain. *GEOPHYSICS* 81:5, S299-S315. [[Abstract](#)] [[Full Text](#)] [[PDF](#)] [[PDF w/Links](#)]
32. Yike Liu, Xuejian Liu, Yu Shao, Are Osen, Yingcai Zheng, Hao Hu. Least-squares reverse time migration of controlled order multiples 4240-4244. [[Abstract](#)] [[Enhanced Abstract](#)] [[PDF](#)] [[PDF w/Links](#)] [[Supplementary Material](#)]
33. Yuting Duan, Paul Sava, Antoine Guittot. Elastic least-squares reverse time migration 4152-4157. [[Abstract](#)] [[Enhanced Abstract](#)] [[PDF](#)] [[PDF w/Links](#)] [[Supplementary Material](#)]
34. Xuejian Liu, Yike Liu, Huiyi Lu, Hu Hao. Prestack-image based correlative least-squares reverse time migration 4466-4470. [[Abstract](#)] [[Enhanced Abstract](#)] [[PDF](#)] [[PDF w/Links](#)]
- 35.. Seismic Processing: Migration I Complete Session 4145-4315. [[Abstract](#)] [[PDF](#)] [[PDF w/Links](#)]
- 36.. Seismic Processing: Migration II Complete Session 4316-4480. [[Abstract](#)] [[PDF](#)] [[PDF w/Links](#)]
- 37.. Technical Program in full - Part II (RC 1 - VSP P1) 2770-5637. [[Crossref](#)]
38. Kyle Basler-Reeder, John Louie, Satish Pullammanappallil, Graham Kent. 2016. Joint optimization of vertical component gravity and P-wave first arrivals by simulated annealing. *GEOPHYSICS* 81:4, ID59-ID71. [[Abstract](#)] [[Full Text](#)] [[PDF](#)] [[PDF w/Links](#)]
39. Chong Zeng, Shuqian Dong, Bin Wang. 2016. Adaptive least-squares RTM with applications to subsalt imaging. *The Leading Edge* 35:3, 253-257. [[Abstract](#)] [[Full Text](#)] [[PDF](#)] [[PDF w/Links](#)]
40. Jizhong Yang*, Yuzhu Liu, Liangguo Dong. Frequency domain least-squares reverse time migration with a modified scattering-integral approach 4164-4169. [[Abstract](#)] [[Enhanced Abstract](#)] [[PDF](#)] [[PDF w/Links](#)]